nature materials

ARTICLES

https://doi.org/10.1038/s41563-019-0531-0

Dirac fermions and flat bands in the ideal kagome metal FeSn

Mingu Kang[1,12], Linda Ye[1,12], Shiang Fang[2], Jhih-Shih You[3], Abe Levitan[1], Minyong Han[1], Jorge I. Facio[3], Chris Jozwiak[4], Aaron Bostwick[4], Eli Rotenberg[4], Mun K. Chan[5], Ross D. McDonald[5], David Graf[6], Konstantine Kaznatcheev[7], Elio Vescovo[7], David C. Bell[8,9], Efthimios Kaxiras[2,8], Jeroen van den Brink[3], Manuel Richter[3,10], Madhav Prasad Ghimire[3,11], Joseph G. Checkelsky[1*] and Riccardo Comin[1*]

A kagome lattice of 3*d* transition metal ions is a versatile platform for correlated topological phases hosting symmetry-protected electronic excitations and magnetic ground states. However, the paradigmatic states of the idealized two-dimensional kagome lattice—Dirac fermions and flat bands—have not been simultaneously observed. Here, we use angle-resolved photoemission spectroscopy and de Haas–van Alphen quantum oscillations to reveal coexisting surface and bulk Dirac fermions as well as flat bands in the antiferromagnetic kagome metal FeSn, which has spatially decoupled kagome planes. Our band structure calculations and matrix element simulations demonstrate that the bulk Dirac bands arise from in-plane localized Fe-3*d* orbitals, and evidence that the coexisting Dirac surface state realizes a rare example of fully spin-polarized two-dimensional Dirac fermions due to spin-layer locking in FeSn. The prospect to harness these prototypical excitations in a kagome lattice is a frontier of great promise at the confluence of topology, magnetism and strongly correlated physics.

The kagome lattice is a two-dimensional (2D) network of corner-sharing triangles (Fig. 1a) that originally gained the spotlight as a platform for frustration-driven exotic spin-liquid phases[1,2]. Recent theoretical investigations have focused on the emergent electronic excitations engendered by the special geometry of the kagome network, whose unique combination of lattice symmetry, spin–orbit coupling, and unusual magnetism sets an ideal stage for novel topological phases[3–8]. Viewed as an isolated layer, the kagome lattice hosts a flat band and a pair of Dirac bands as depicted in the nearest-neighbour tight-binding calculation in Fig. 1b (refs. [3,4]). Compounded with spin–orbit coupling and a net magnetization, the 2D kagome lattice realizes a 2D Chern insulator phase with quantized anomalous Hall conductance at 1/3 and 2/3 fillings[5]. When these quantum anomalous Hall layers are stacked along the third dimension, the interlayer interaction drives the mass gap to be closed and reopened along the stacking axis, transforming the system into a three-dimensional (3D) magnetic Weyl semimetal[7,9]. Focusing on a flat band with quenched kinetic energy, interaction-driven many-body electronic phases ranging from density waves to superconductivity have been theoretically investigated[10]. At the same time, the flat band on the kagome lattice also carries a finite Chern number, and mimics the phenomenology of Landau levels, without an external magnetic field[8,11]. As a result, the fractional quantum Hall state can be realized at a partial filling of these flat bands, further enriching the spectrum of topological phases that can be harnessed within the kagome lattice.

These promising theoretical proposals have driven and guided recent experimental efforts toward the realization and study of topological kagome metals based on binary and ternary intermetallic compounds[12–23]. At variance with other widely studied *s* or *p* orbital-based toplogical systems that are close to the non-interacting limit, the kagome lattice in these intermetallic materials is populated by the low-energy 3*d* electrons of transition metals (Fig. 1a), and thus provide an ideal platform to study the interplay of electronic topology and strong correlations. Correspondingly, not only topological electronic structures but also rich intrinsic magnetism can be found in the 3*d* kagome metal series. The combination of these two aspects gives rise to intrinsic anomalous Hall conductivity via various mechanisms[12,14,16,20,21].

Despite the great potential and rich phenomenology of this family of materials, the experimental realization of the electronic structure of an idealized 2D kagome lattice, namely the Dirac fermions and topological flat bands (Fig. 1b), in bulk magnetic kagome crystals has remained an outstanding challenge. For instance, in the binary intermetallic T_mX_n kagome series (T = Mn, Fe, Co; X = Sn, Ge; m:n = 3:1, 3:2, 1:1) with various stacking sequences of kagome and spacer S layers (Fig. 1c–e), the quasi-2D Dirac electronic structure has been detected only in Fe_3Sn_2 (ref. [16]) but not in Mn_3Sn (ref. [14]). Rather, in Mn_3Sn and ternary kagome compound $Co_3Sn_2S_2$, 3D magnetic Weyl points have been identified as the potential origin for the chiral anomaly in transport[14,20], as also confirmed by band structure calculations[7,20–22]. For what concerns the flat bands,

[1]Department of Physics, Massachusetts Institute of Technology, Cambridge, MA, USA. [2]Department of Physics, Harvard University, Cambridge, MA, USA. [3]Leibniz Institute for Solid State and Materials Research, IFW Dresden, Dresden, Germany. [4]Advanced Light Source, E. O. Lawrence Berkeley National Laboratory, Berkeley, CA, USA. [5]National High Magnetic Field Laboratory, Los Alamos National Laboratory, Los Alamos, NM, USA. [6]National High Magnetic Field Laboratory, Tallahassee, FL, USA. [7]National Synchrotron Light Source II, Brookhaven National Laboratory, Upton, NY, USA. [8]John A. Paulson School of Engineering and Applied Sciences, Harvard University, Cambridge, MA, USA. [9]Center for Nanoscale systems, Harvard University, Cambridge, MA, USA. [10]Dresden Center for Computational Materials Science (DCMS), TU Dresden, Dresden, Germany. [11]Central Department of Physics, Tribhuvan University, Kirtipur, Kathmandu, Nepal. [12]These authors contributed equally: Mingu Kang, Linda Ye. *e-mail: checkelsky@mit.edu; rcomin@mit.edu

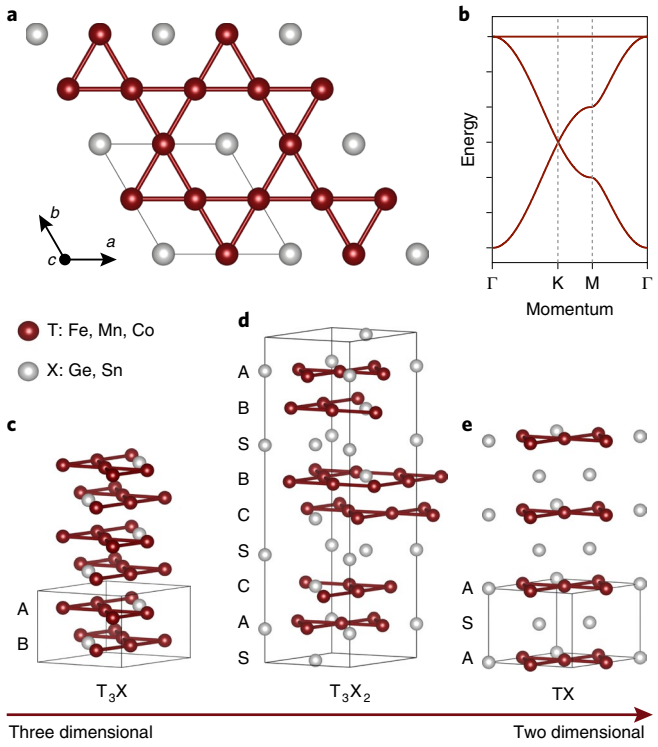

Fig. 1 | Crystal structure of binary kagome metals. a, Top view of the kagome plane in binary kagome metals T_mX_n. The kagome network consists of 3*d* transition metal atoms (T: Fe, Mn, Co) with space-filling atoms (X: Sn, Ge) at the centre of the hexagon. The in-plane unit cell is marked with the parallelogram. **b**, Tight-binding band structure of kagome lattice exhibiting two Dirac bands at the K point and a flat band across the whole Brillouin zone. **c**–**e**, Stacking sequences of the binary kagome metal series T_mX_n with $m{:}n = 3{:}1$ (**c**), 3:2 (**d**) and 1:1 (**e**). Structural unit cells are marked with a solid line. The kagome layers labelled with A–C have different in-plane lattice offsets. Spacing layers consisting of X atoms in a hexagonal arrangement are labelled with S. The structural two-dimensionality increases with increasing ratio of X to T. In the TX (1:1) structure (**e**), the kagome layers are perfectly aligned with one another and are interleaved with S layers, while in the T_3X structure (**c**), neighbouring kagome layers are directly stacked without spacing layers. In the T_3X_2 structure (**d**), both types of stacking coexist.

a diverging density of states was found in Fe_3Sn_2 and $Co_3Sn_2S_2$ using scanning tunneling spectroscopy; however, no signatures of these nondispersive excitations in momentum space have been reported so far, presumably due to the complex interlayer interactions, disrupting flat bands in the 2D kagome limit (Fig. 1d)[19,23]. Given the premises, the investigation of a material with a simpler stacking structure is desired to provide a prototypical realization of the electronic structure of the kagome lattice.

In this study, we report the electronic structure of kagome metal FeSn, unique among its T_mX_n sibling compounds in that it is based on isolated and spatially decoupled kagome planes (Fig. 1e, see Methods and Supplementary Fig. 1 for details on synthesis and characterizations). Compared to the previously studied Mn_3Sn and Fe_3Sn_2 structures (Fig. 1c,d), FeSn has one kagome layer in the unit cell, and is the compound closest to the 2D limit owing to the large separation between the neighbouring kagome layers (Fig. 1e). This sets an ideal stage to investigate the electronic structure of the 2D kagome network in a bulk crystal. FeSn is magnetically ordered, with Fe moments ferromagnetically aligned within each kagome plane but antiferromagnetically coupled along the *c*-axis[24]. This magnetic state allows for a simple hopping model, free from the complications of a non-collinear magnetic texture as instead is found in Mn_3Sn-type kagome antiferromagnets[12]. As detailed below, our comprehensive study of the electronic structure of FeSn—combining angle-resolved photoemission spectroscopy (ARPES), magneto-quantum oscillations, and density functional theory (DFT) calculations—reveals the rich phenomenology of the kagome lattice in its full variety, featuring the coexistence of bulk and surface Dirac fermions, as well as the long sought-after flat bands.

Termination-dependent ARPES experiments

In Fig. 2, we summarize our photoemission experiments on FeSn. We first note that FeSn can expose two possible surface terminations upon cleaving, namely the kagome and Sn terminations marked as A and S in Fig. 1e. We determined that the surface termination can be uniquely identified in situ using X-ray photoelectron spectroscopy (XPS) on Sn 4*d* core levels as shown in Fig. 2a,b (see also Methods and Supplementary Figs. 2 (detailed analysis of XPS spectra), 3 (DFT analysis of surface level shifts) and 4 (atomic force microscopy characterization of the surface terminations)), and measured valence band structure on both terminations. Interestingly, our ARPES data uncover a strong dependence of the valence band structure on surface termination. In Fig. 2d,f, we first present the Fermi surface (Fig. 2d) and energy-momentum dispersion (Fig. 2f) from the kagome termination. The most prominent feature on the Fermi surface is a circular electron pocket (dashed circle in Fig. 2d) centred at the corner of the hexagonal Brillouin zone (K point), which arises out of the Dirac bands expected from the kagome tight-binding model (Fig. 1b) and previously observed in Fe_3Sn_2 (ref. [16]). The energy–momentum dispersion across the K point (Fig. 2f) confirms the presence of a clear Dirac cone structure (DC1) with linear crossing at $E_{D1} = -0.43 \pm 0.02$ eV. To closely visualize the momentum-space structure of the Dirac bands, we show a series of constant energy maps in Fig. 2g–j, measured at +0.4 eV, +0.2 eV, 0 eV and −0.2 eV with respect to E_{D1}. Far above E_{D1}, the large electron pocket centred at the K point (Fig. 2g) can be seen, which shrinks to a single Dirac point (Fig. 2i) and reopens (Fig. 2j) linearly as the energy crosses E_{D1}. The velocity of Dirac fermions in FeSn is $(1.7 \pm 0.2) \times 10^5$ m s^{-1}, an order of magnitude lower than that of graphene and in close range of that of Fe_3Sn_2 (ref. [16]) and Fe-based superconductors[25–27], possibly reflecting the more localized nature of Fe-3*d* electrons. Overall, our ARPES data directly establish the Dirac fermiology in kagome antiferromagnet FeSn, which could be harnessed for topological antiferromagnetic spintronics.

The electronic structure measured on the Sn termination is even richer than that on the kagome termination, as shown in Fig. 2c,e. The Fermi surface (Fig. 2c) exhibits a triangular electron pocket centred at the K point in addition to the circular pocket from DC1. The band dispersion shown in Fig. 2e reveals that the new pocket arises from a second Dirac cone (DC2) with crossing at $E_{D2} = -0.31 \pm 0.02$ eV. The binding energy and dispersion of DC1 is unaltered on this termination. Further, DC1 and DC2 exhibit very different trigonal warping patterns away from the Dirac point (black dashed circle and triangle in Fig. 2c), despite their similar Dirac velocities. This aspect hints at the different origin of the two Dirac bands, and rules out other scenarios, such as layer-splitting, quantum-well states[28] or bosonic shake-off replicas[29]. Instead, the inequivalence of the electronic spectra from the two terminations provides a direct insight on the nature of DC1 and DC2: the former is a bulk Dirac band that manifests itself independently of the surface termination, while the latter represents a surface Dirac state that is observed only on the Sn termination. Photon energy-dependent ARPES measurements further reveal that the dispersions of DC1 and DC2 are unaltered along the out-of-plane direction (Supplementary Fig. 5), reflecting the 2D nature of Dirac fermions in FeSn. The 2D kagome-derived electronic structure of FeSn is consistent with that expected from

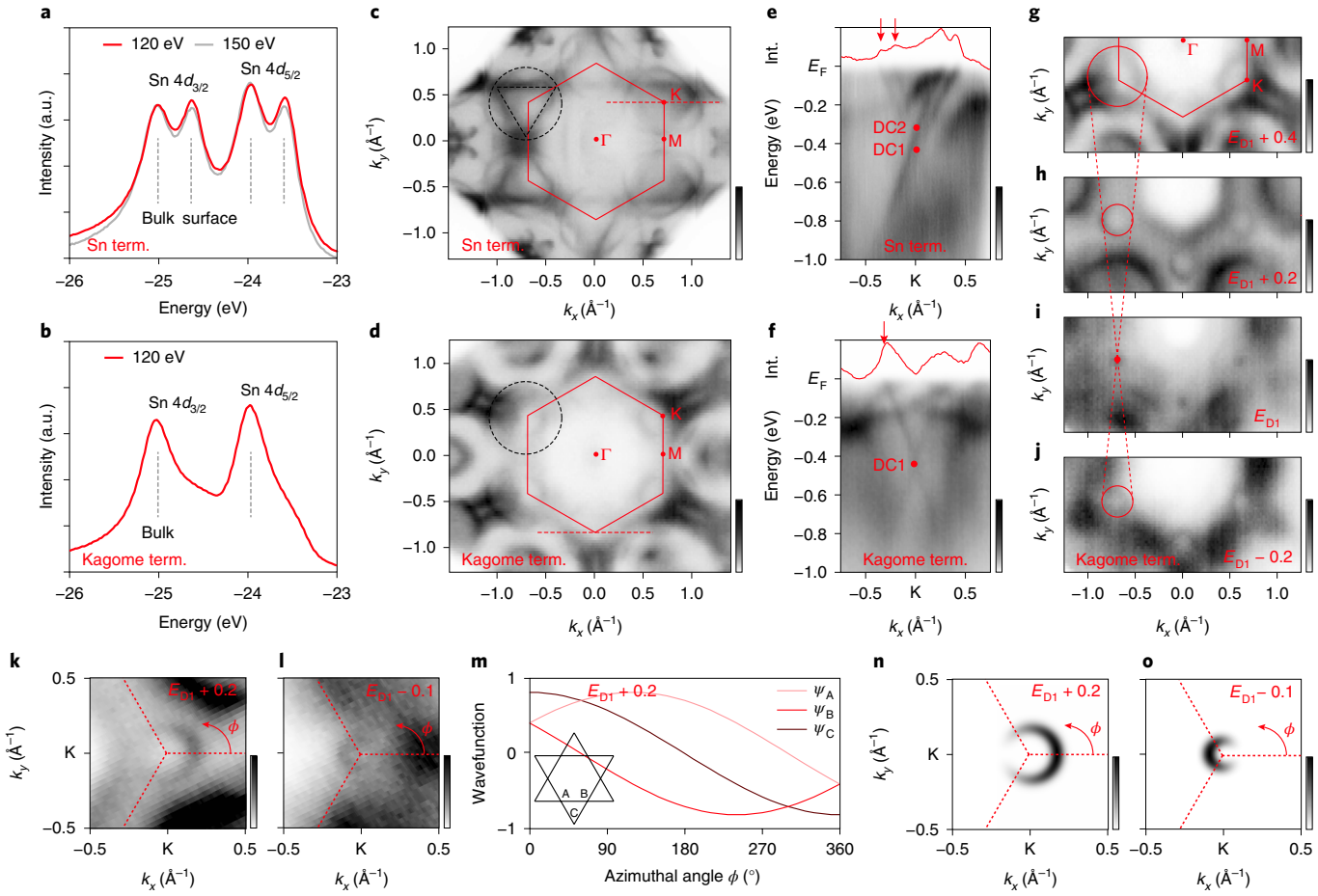

Fig. 2 | Photoemission experiments on FeSn. a,**b**, Two representative XPS spectra of in situ cleaved FeSn, from which we identified the surface termination as Sn and kagome layers, respectively for **a** and **b**. **c**,**d**, Fermi surfaces of FeSn measured on Sn and kagome terminations, respectively for **c** and **d**. The Brillouin zone is marked with the red solid hexagon. The dashed black circle and triangle schematically represent the prominent Fermi surfaces centred at the K point. **e**,**f**, Energy–momentum dispersion of FeSn across the K point along the dashed red line marked in **c**,**d**. DC1 and DC2 indicate the position of Dirac points. Momentum distribution curves at Fermi energy are overlaid, with arrows indicating peaks at k_F. Int., intensity. **g**–**j**, Constant energy maps measured on the kagome termination at +0.4 eV, +0.2 eV, 0 eV and −0.2 eV with respect to the E_{D1}, with clear shrinking and reopening of the Dirac pocket as the energy crosses the Dirac point. **k**,**l**, Constant energy map above and below DC1, respectively, highlighting the modulation of the photoemission intensity around the Dirac point. **m**, Dirac wave function on three sublattices of the kagome lattice featuring Berry phase π acquired after 2π azimuthal rotation. **n**,**o**, Simulation of sublattice interference pattern of kagome lattice from Dirac wave functions in **m**. Colour bar at the bottom right of each panel indicates intensity from minimum (bottom) to maximum (top).

its lattice structure with spatially decoupled kagome layers (Fig. 1e). This characteristic is unique to FeSn and represents the opposite limit to the case of all-kagome compound Mn_3Sn (Fig. 1c), where an overall 3D electronic structure without any signature of 2D Dirac cones has been observed[14].

dHvA and SdH quantum oscillation experiments

The surface versus bulk origin of the two Dirac bands can be further pinned down using a bulk sensitive probe of the electronic structure: here we focus on the de Haas–van Alphen (dHvA) effect, which as a thermodynamic quantity exclusively measures the quantized Landau level formation of bulk Fermi surfaces. Using torque magnetometry at high magnetic fields and low temperatures (see Methods), we resolve dHvA oscillations (see Supplementary Fig. 6) with frequencies summarized in Fig. 3a as circles. Multiple frequencies are observed that vary systematically as a function of field orientation with respect to the kagome plane normal (θ, see inset of Fig. 3a). Magnetoresistance Shubnikov–de Haas (SdH) oscillations are also observed (see Supplementary Fig. 7) whose frequencies are a subset of the dHvA frequencies, marked as triangles in Fig. 3a. We index these branches as $\alpha_{1,2,3}$, $\beta_{1,2}$, $\gamma_{1,2}$ and δ based on their qualitative evolution with θ. Most importantly, the frequencies of the β, γ and δ bands remain finite during a complete θ rotation, while the α band frequency diverges as $(\cos\theta)^{-1}$ as the magnetic field is tilted toward the kagome plane. The former behaviour is a characteristic of 3D closed Fermi pockets, while the latter is indicative of quasi-2D Fermi sheets (for an ideal 2D Fermi surface, a $f(\theta) = f_0(\cos\theta)^{-1}$ dependence is expected where f_0 is proportional to the area of the Fermi surface, A_F). The values of f_0 (A_F) extracted from the fit (dashed lines in Fig. 3a) are 1,310 T (0.125 Å^{-2}), 3,642 T (0.348 Å^{-2}) and 6,755 T (0.656 Å^{-2}) for α_1, α_2 and α_3, respectively. To further characterize these Fermi surfaces, we show in Fig. 3b the damping of the quantum oscillation amplitudes with elevated temperature fitted with a Lifshitz–Kosevich formula (see Methods). The obtained effective masses m^* of the α_1, α_2 and α_3 bands are $(5.4 \pm 0.4)m_e$, $(3.1 \pm 0.2)m_e$ and $(4.3 \pm 0.3)m_e$, respectively.

To validate the correspondence between the observations from ARPES and quantum oscillations, we compare the experimental

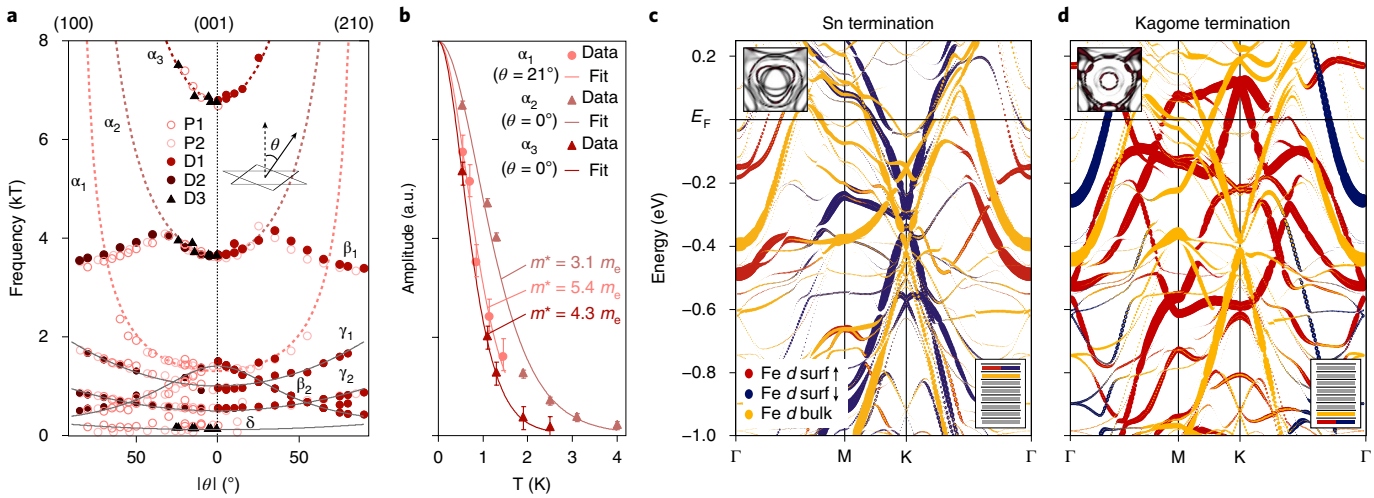

Fig. 3 | Magneto-quantum oscillations and slab DFT calculations of FeSn. a, Angular dependence of dHvA (circles) and SdH (triangles) oscillation frequencies of FeSn. Hollow symbols indicate the frequencies obtained from pulsed field measurement, while filled symbols indicate those obtained from DC field measurement. Different colours indicate different samples. The inset schematically represents the definition of θ with respect to the kagome plane normal. Dashed lines indicate the fit of α bands to the $\cos(\theta)^{-1}$ function, the behaviour expected from a quasi 2D Fermi surface. **b**, Temperature dependence of quantum oscillation (dHvA for α_1, SdH for α_2 and α_3) amplitude of α bands. Solid lines are fit to the Lifshitz–Kosevich formula (see Methods). All curves are normalized to the expected zero-temperature value. **c**,**d**, Slab DFT calculations of eight FeSn structural unit cells. Bottom-right insets show schematic structure of the slab with black lines representing Sn layers and rectangles representing kagome layers. Red and blue circles represent the weight of spin up and down states on topmost kagome layers ('surf'), while orange circles represent the weight of states on the second topmost kagome layers ('bulk'). The top-left insets in **c**,**d** show the Fermi contours of Dirac pockets around the K point, which capture the anisotropic warping of bulk (DC1) and surface (DC2) Dirac cones (see Fig. 2c,d for comparison).

Table 1 | Comparison of ARPES and quantum oscillation experiments and DFT calculations on FeSn

ARPES

	A_F (Å^{-2})	v_F (10^5 m s^{-1})	E_D (eV)
Dirac cone 1 (DC1, bulk)	**0.38 ± 0.03**	**1.70 ± 0.20**	0.43 ± 0.02
Dirac cone 2 (DC2, surface)	0.26 ± 0.02	1.87 ± 0.20	0.31 ± 0.02

Quantum oscillation

	f_0 (T)	m^* (m_e)	A_F (Å^{-2})	$v_F = \sqrt{\frac{E_{D1}}{m^*}}(\cos\theta)^{-1}$ (10^5 m s^{-1})	$v_F = \sqrt{\frac{E_{D2}}{m^*}}(\cos\theta)^{-1}$ (10^5 m s^{-1})
α_1	1,310 ± 2	5.4 ± 0.4	0.1251 ± 0.0002	1.17 ± 0.07	1.04 ± 0.05
α_2 (corresponds to DC1)	3,641.5 ± 0.1	3.1 ± 0.2	**0.34761 ± 0.00001**	**1.54 ± 0.09**	1.34 ± 0.09
α_3	6,755.3 ± 0.8	4.3 ± 0.3	0.65586 ± 0.00008	1.31 ± 0.08	1.13 ± 0.08

DFT

	A_F (Å^{-2})	v_F (10^5 m s^{-1})	E_D (eV)
DC1 (bulk)	0.19	2.70	0.41
DC1 (slab)	0.20	2.55	0.42
DC2 (slab)	0.10	2.83	0.28

v_F from ARPES and DFT is calculated from the slope of Dirac bands at the Fermi energy averaged on multiple momentum-space directions to account for the trigonal warping. v_F from quantum oscillation is derived from the effective m^* and E_D as $v_F = \sqrt{\frac{E_D}{m^*}}(\cos\theta)^{-1}$ assuming Dirac dispersion.

parameters of DC1, DC2, α_1, α_2 and α_3 in Table 1. In magneto-quantum oscillations, v_F can be obtained from m^* by assuming a Dirac dispersion[17], that is $v_F = \sqrt{E_F/m^*}$. An excellent agreement in both A_F and v_F is obtained between DC1 and α_2, suggesting that they represent the same band. This equivalence confirms the bulk origin of DC1, whose Landau orbit under high magnetic field appears as α_2 in quantum oscillation experiments. In contrast, both A_F and v_F of DC2 markedly deviate from those of α_1 and α_3, by a factor of almost two. Instead, a close comparison with the calculated dHvA spectrum (Supplementary Fig. 8) suggests that α_1 and α_3 originate from different quasi-2D Fermi surfaces centred at Γ. The absence of a bulk band corresponding to DC2 thus demonstrates its surface origin as inferred from the termination-dependent ARPES spectra above. In sum, by combining complementary photoemission and quantum oscillations experiments, we confirmed the quasi-2D Dirac fermiology of FeSn, and also revealed the unusual coexistence

of surface and bulk Dirac fermions in the single compound. We note that the direct comparison between ARPES and dHvA quantum oscillations is partially enabled by the antiferromagnetic spin structure of FeSn, which is largely unchanged in the applied fields in our dHvA experiments (see Supplementary Sections 1 and 5). For comparison, in the case of the closely related soft-ferromagnetic kagome metal Fe_3Sn_2, the magnetization and band structure change as a function of applied field direction, so that the quantum oscillation of the Dirac bands deviates from the simple 2D form, $f(\theta) = f_0(\cos\theta)^{-1}$ (ref. [18]).

Band structure calculation and matrix element analysis

To understand the origin of surface and bulk Dirac fermions, we extended the tight-binding calculations of the ideal 2D kagome lattice (Fig. 1b) to incorporate the *d*-orbital degrees of freedom. Further, we performed DFT calculations of FeSn in both bulk and slab geometries. In the monolayer kagome tight-binding model with a *d*-orbital basis, five separate Dirac points emerge at the K point from the five 3*d* orbitals (Supplementary Fig. 9). Complementary bulk DFT calculations (Supplementary Fig. 10) reveal that the Dirac points with different orbital characters respond very differently to the interlayer coupling: the Dirac points with in-plane orbital character (d_{xy} and d_{x2-y2}) retain their 2D nature and are unaffected when embedded in the bulk Brillouin zone, while those with out-of-plane orbital character (d_{xz}, d_{yz}, and d_{3z2-r2}) acquire a pronounced k_z dispersion and lose their characteristic 2D kagome features in the bulk model. Accordingly, near the Fermi level our bulk DFT predicts a single 2D Dirac band with $d_{xy}+d_{x2-y2}$ characters at $E \approx -0.4$ eV (Fig. 4a and Supplementary Fig. 10), which closely agrees with the experimentally observed bulk Dirac cone (DC1). The robustness of the 2D Dirac dispersion in the bulk kagome lattice is in stark contrast to the case of graphene, where the Dirac cone with out-of-plane p_z orbital character is strongly susceptible to interlayer interactions and loses its characteristic linear dispersion or 2D nature in multilayer or bulk form[30,31]. These findings suggest that the careful engineering of localized 3*d*-orbital character is a key to realize the desired kagome electronic bands in bulk magnetic kagome crystals.

The surface Dirac band (DC2) is also reproduced in DFT calculations based on a slab geometry. Figure 3c,d displays the band structure of FeSn slabs composed of eight kagome layers terminated with a kagome layer on one side and Sn layer on the other side (schematically shown in the insets of Fig. 3c,d). In this model, the six inner kagome layers mimic the bulk local environment (marked as 'bulk', orange circles), while the outer kagome layers are subject to the surface-shift of exchange and electrostatic potential (see Supplementary Fig. 3) of each termination (marked as 'surf', red and blue circles). For simplicity, in Fig. 3c,d we only weight the second outermost kagome layers as a bulk state, since all six inner kagome layers are essentially degenerate in terms of Dirac bands (see Supplementary Fig. 11). First, one finds a termination-independent Dirac cone (orange) arising from the bulk kagome layers at $E \approx -0.4$ eV, which corresponds to DC1 in bulk DFT and ARPES. At the same time, an additional Dirac band (blue) localized within the surface kagome layer emerges at $E \approx -0.3$ eV in the Sn-terminated slab, which closely reproduces the DC2 band observed by ARPES (see Fig. 2e). The orbital analysis presented in Supplementary Fig. 11 reveals that the surface Dirac state (DC2) possesses an identical orbital character ($d_{xy}+d_{x2-y2}$) to the bulk Dirac state (DC1), indicating that DC2 is a surface resonant state emerging from DC1 under the surface potential. The surface state is strongly localized on the topmost kagome layer, wherein the spins are ferromagnetically aligned under the intrinsic 'A-type' antiferromagnetism of FeSn. Therefore, the surface state (DC2) of FeSn realizes a rare example of fully spin-polarized 2D Dirac fermions (Fig. 3c), which far surpasses, for example, the partial (~25%) spin-polarization in the graphene/ferromagnet heterostructures[32], and is highly desirable for realizing fast-switching/low-power spintronic devices, spin-superconductors[33] and a high-temperature quantum anomalous Hall effect. Lastly, despite the success of DFT in reproducing the energy and termination dependence of the bulk and surface Dirac cones, the theoretical Dirac fermion velocity needs to be slightly renormalized by a factor of 0.6 to match the experimental value (see the Table 1 for comparison), suggesting possible electronic correlation effects in FeSn.

The simple structure of FeSn also enables a detailed analysis of the photoemission intensity pattern of the kagome-derived Dirac cone, which conveys the phase information of the initial state wavefunction. Such analysis has been previously used to uncover helical spin textures and chirality of Dirac fermions in 3D topological insulators and graphene[34–36], but has never been applied to a kagome lattice. As shown in Fig. 2k,l, the photoemission intensity is strongly modulated around the Dirac cone, a direct consequence of phase interference between wave functions from different kagome sublattices. The intensity modulation follows a $\cos\phi$ function (where ϕ is an azimuthal rotation angle around the Dirac cone), with both maximum and minimum along the Γ-K direction but at opposite momenta above (Fig. 2k) and below (Fig. 2l) the Dirac point, identical to the case of graphene[35,36]. As shown in Fig. 2n,o, our simulation based on sublattice interference of kagome initial state wavefunctions with Berry phase π (Fig. 2m) closely reproduces this intensity pattern, demonstrating the chirality of kagome-derived Dirac fermions in FeSn (see Supplementary information for details).

Signature of kagome-derived flat bands

Having fully characterized the kagome-derived Dirac states, we also searched for the flat bands in FeSn, the other defining feature of an ideal kagome lattice. Despite surging theoretical interest on the physics of flat bands[8,37,38], their direct signatures have been elusive: for example, flat bands reported in other kagome systems including Fe_3Sn_2 and $Co_3Sn_2S_2$ were confined to subregions of the Brillouin zone possibly due to the complex interlayer interactions in these systems[19,23]. Based on our orbital analysis above, we could infer that FeSn might be an ideal system where flat bands constructed from in-plane *d* orbitals are invulnerable to interlayer interactions and retain their nondispersive character in momentum-space. Accordingly, our bulk DFT calculation reveals quasi-2D nearly flat bands (with the bandwidth about 1/5 of that of the Dirac bands) with d_{xy} and d_{x2-y2} characters at about 0.5 eV above Fermi level (see Supplementary Figs. 10 and 4a). In combination with the observed Dirac cone structure, the complete prototypical kagome band structure of Fig. 1b could be thus realized or mimicked in FeSn using electronic bands derived from in-plane 3*d* orbitals.

The aforementioned quasi-2D nearly flat band cannot be directly observed by ARPES as it lies above the Fermi level. Instead, we can search for a signature of flat bands from other *d*-orbital degrees of freedom, which can arise at various energies (see Supplementary Fig. 9 for *d*-orbital-based kagome tight-binding model). Figure 4b,c displays the experimental band structures of FeSn along Γ-K-M high symmetry directions measured with linear horizontal (LH) and linear vertical (LV) polarizations, respectively for Fig. 4b and Fig. 4c. The signature of flat bands is absent under LH polarization, while LV polarization reveals a strikingly nondispersive excitation near the Fermi level ($E_{flat} = -0.23 \pm 0.05$ eV). Accordingly, as shown in the constant energy map at E_{flat} in Fig. 4d, the spectral weight of this band is uniformly distributed across almost the full 2D Brillouin zone except around the K points due to the intensity leakage from the Dirac bands. This observation represents the first momentum-space evidence of the flat band in the kagome system. The experimental bandwidth of the flat band is less than 1/10 of that of the Dirac bands and comparable to what has been observed in *f*-electron systems[39]. Unlike the latter cases, however, the kagome-derived flat band arises from a destructive phase interference of

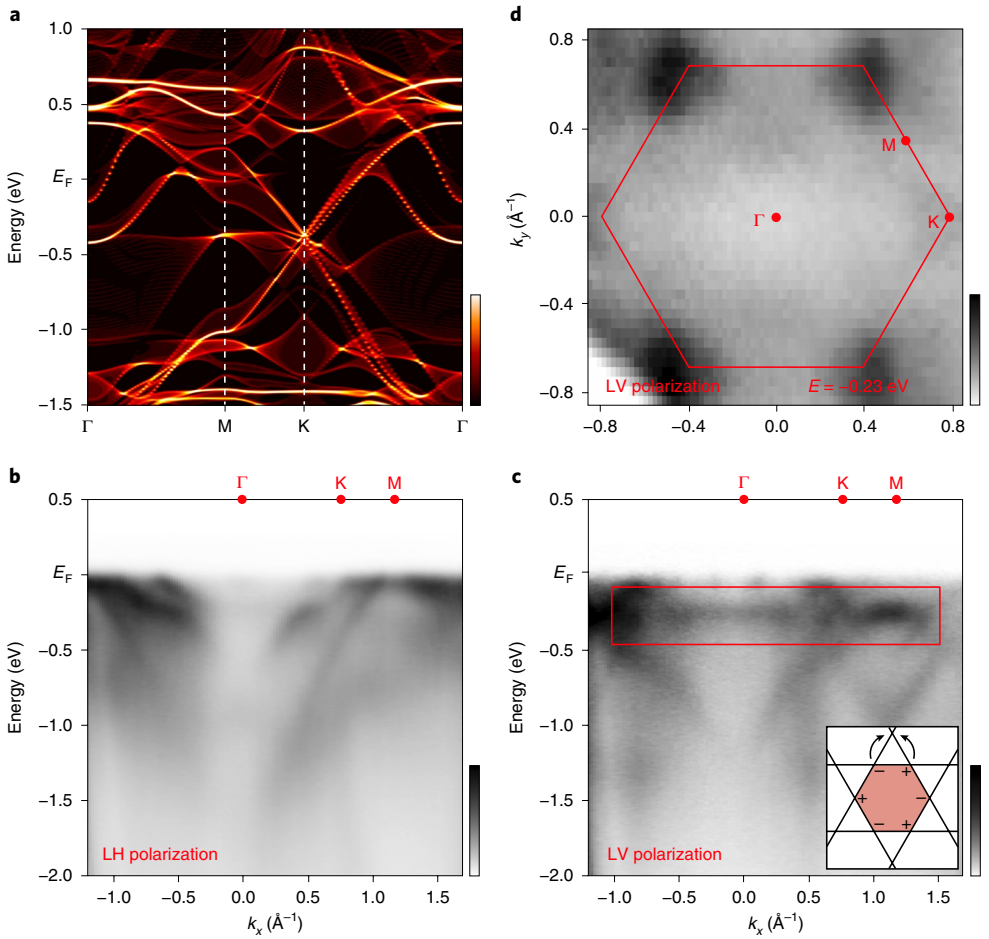

Fig. 4 | Signature of flat bands in FeSn. a, Energy-momentum dispersion of FeSn integrated along the out-of-plane momentum (k_z). **b**,**c**, Experimental band structures of FeSn along the Γ-K-M high symmetry directions measured with LH and LV polarizations (incident photon polarization in to and out of the photoelectron emission plane, respectively) on kagome termination. The red box in **c** highlights the nearly flat band around E_{flat} = –0.23 eV. The inset in **c** depicts the confinement of an electron in the hexagon of the kagome lattice arising from the destructive phase interference between hoppings from different sublattices. **d**, Constant energy map of FeSn at E_{flat} highlighting the almost uniform intensity distribution from the nondispersive band (the higher intensity at a few of the K points is due to the presence of the Dirac band in the same energy range).

hopping in a frustrated geometry (inset of Fig. 4c), and is thus intrinsically topological with finite spin–orbit coupling[11]. In real space, this phase interference effectively localizes the wavefunction into a single hexagon as depicted in the inset of Fig. 4c. Such localization to the subregion of real space is similar to the case of the engineered flat band in the magic-angle twisted bilayer graphene, with an electron localized to the AA-stacked region of the Moiré superlattice[40]. Comparing the length scale of localization d, the kagome lattice (in the ideal case) evidently promotes a stronger localization ($d \approx 5$ Å) than the Moiré superlattice ($d \approx 50$ Å), which directly implies a stronger effective Coulomb energy scale by $U = e^2/4\pi\epsilon d$. The identification of the flat band opens up important opportunities for engineering new correlated electron phases in the kagome lattice via local electrostatic gates (tuning the flat bands to the Fermi level) and by controlling the strength of magnetic exchange splitting. Altogether, our discovery and extensive analysis of the Dirac cone and flat bands in the ideal kagome metal FeSn unlock new perspectives and avenues for the realization of correlated topological phases and spintronic devices based on kagome lattices.

Online content

Any methods, additional references, Nature Research reporting summaries, source data, extended data, supplementary information, acknowledgements, peer review information; details of author contributions and competing interests; and statements of data and code availability are available at https://doi.org/10.1038/s41563-019-0531-0.

Received: 5 June 2019; Accepted: 8 October 2019;
Published online: 9 December 2019

References

1. Sachdev, S. Kagome- and triangular-lattice Heisenberg antiferromagnets: ordering from quantum fiuctuations and quantum-disordered ground states with unconfined bosonic spinons. *Phys. Rev. B* **45**, 12377–12396 (1992).
2. Balents, L. Spin liquids in frustrated magnets. *Nature* **464**, 199–208 (2010).
3. Guo, H. M. & Franz, M. Topological insulator on the kagome lattice. *Phys. Rev. B* **80**, 113102 (2009).
4. Mazin, I. I. et al. Theoretical prediction of a strongly correlated Dirac metal. *Nat. Commun.* **5**, 4261 (2014).
5. Xu, G., Lian, B. & Zhang, S.-C. Intrinsic quantum anomalous Hall effect in the kagome lattice $Cs_2LiMn_3F_{12}$. *Phys. Rev. Lett.* **115**, 186802 (2015).
6. Chen, H., Niu, Q. & Macdonald, A. H. Anomalous hall effect arising from noncollinear antiferromagnetism. *Phys. Rev. Lett.* **112**, 17205 (2014).
7. Kübler, J. & Felser, C. Non-collinear antiferromagnets and the anomalous Hall effect. *Europhys. Lett.* **108**, 67001 (2014).
8. Tang, E., Mei, J.-W. & Wen, X.-G. High-temperature fractional quantum Hall states. *Phys. Rev. Lett.* **106**, 236802 (2011).
9. Burkov, A. A. & Balents, L. Weyl semimetal in a topological insulator multilayer. *Phys. Rev. Lett.* **107**, 127205 (2011).

10. Wen, J., Rüegg, A., Wang, C. C. J. & Fiete, G. A. Interaction-driven topological insulators on the kagome and the decorated honeycomb lattices. *Phys. Rev. B* **82**, 75125 (2010).
11. Bolens, A. & Nagaosa, N. Topological states on the breathing kagome lattice. *Phys. Rev. B* **99**, 165141 (2019).
12. Nakatsuji, S., Kiyohara, N. & Higo, T. Large anomalous Hall effect in a non-collinear antiferromagnet at room temperature. *Nature* **527**, 212–215 (2015).
13. Nayak, A. K. et al. Large anomalous Hall effect driven by non-vanishing Berry curvature in non-collinear antiferromagnet Mn_3Ge. *Sci. Adv.* **2**, e1501870 (2016).
14. Kuroda, K. et al. Evidence for magnetic Weyl fermions in a correlated metal. *Nat. Mater.* **16**, 1090–1095 (2017).
15. Liu, Z. Q. et al. Electrical switching of the topological anomalous Hall effect in a non-collinear antiferromagnet above room temperature. *Nat. Electron.* **1**, 172–177 (2018).
16. Ye, L. et al. Massive Dirac fermions in a ferromagnetic kagome metal. *Nature* **555**, 638–642 (2018).
17. Yin, J. X. et al. Giant and anisotropic many-body spin–orbit tunability in a strongly correlated kagome magnet. *Nature* **562**, 91–95 (2018).
18. Ye, L. et al. De Haas–van Alphen effect of correlated Dirac states in kagome metal Fe_3Sn_2. *Nat. Commun.* **10**, 4870 (2019).
19. Lin, Z. et al. Flatbands and emergent ferromagnetic ordering in Fe_3Sn_2 kagome lattices. *Phys. Rev. Lett.* **121**, 96401 (2018).
20. Liu, E. et al. Giant anomalous Hall effect in a ferromagnetic kagome-lattice semimetal. *Nat. Phys.* **14**, 1125–1131 (2018).
21. Wang, Q. et al. Large intrinsic anomalous Hall effect in half-metallic ferromagnet $Co_3Sn_2S_2$ with magnetic Weyl fermions. *Nat. Commun.* **9**, 3681 (2018).
22. Ghimire, M. P. et al. Creating Weyl nodes and controlling their energy by magnetization rotation. Preprint at https://arxiv.org/abs/1903.03179 (2019).
23. Yin, J.-X. et al. Negative flat band magnetism in a spin–orbit-coupled correlated kagome magnet. *Nat. Phys.* **15**, 443–448 (2019).
24. Hartmann, O. & Wappling, R. Muon spin precession in the hexagonal antiferromagnet FeSn. *Phys. Scr.* **35**, 499–503 (1987).
25. Richard, P. et al. Observation of Dirac cone electronic dispersion in $BaFe_2As_2$. *Phys. Rev. Lett.* **104**, 137001 (2010).
26. Tan, S. Y. et al. Observation of Dirac cone band dispersions in FeSe thin films by photoemission spectroscopy. *Phys. Rev. B* **93**, 104513 (2016).
27. Zhang, P. et al. Observation of topological superconductivity in iron-based superconductor. *Science* **360**, 182–186 (2018).
28. Chiang, T. Photoemission studies of quantum well states in thin films. *Surf. Sci. Rep.* **39**, 181–235 (2000).
29. Moser, S. et al. Tunable polaronic conduction in anatase TiO_2. *Phys. Rev. Lett.* **110**, 196403 (2013).
30. Ohta, T., Bostwick, A., Seyller, T., Horn, K. & Rotenberg, E. Controlling the electronic structure of bilayer graphene. *Science* **313**, 951–954 (2006).
31. Zhou, S. Y. et al. First direct observation of Dirac fermions in graphite. *Nat. Phys.* **2**, 595–599 (2006).
32. Marchenko, D. et al. Highly spin-polarized Dirac fermions at the graphene/Co interface. *Phys. Rev. B* **91**, 235431 (2015).
33. Sun, Q. F., Jiang, Z. T., Yu, Y. & Xie, X. C. Spin superconductor in ferromagnetic graphene. *Phys. Rev. B* **84**, 214501 (2011).
34. Wang, Y. H. et al. Observation of a warped helical spin texture in Bi_2Se_3 from circular dichroism angle-resolved photoemission spectroscopy. *Phys. Rev. Lett.* **107**, 207602 (2011).
35. Hwang, C. et al. Direct measurement of quantum phases in graphene via photoemission spectroscopy. *Phys. Rev. B* **84**, 125422 (2011).
36. Liu, Y., Bian, G., Miller, T. & Chiang, T. C. Visualizing electronic chirality and Berry phases in graphene systems using photoemission with circularly polarized light. *Phys. Rev. Lett.* **107**, 166803 (2011).
37. Neupert, T., Santos, L., Chamon, C. & Mudry, C. Fractional quantum Hall states at zero magnetic field. *Phys. Rev. Lett.* **106**, 236804 (2011).
38. Sun, K., Gu, Z., Katsura, H. & Das Sarma, S. Nearly flatbands with nontrivial topology. *Phys. Rev. Lett.* **106**, 236803 (2011).
39. Patil, S. et al. ARPES view on surface and bulk hybridization phenomena in the antiferromagnetic Kondo lattice $CeRh_2Si_2$. *Nat. Commun.* **7**, 11029 (2016).
40. Cao, Y. et al. Correlated insulator behaviour at half-filling in magic-angle graphene superlattices. *Nature* **556**, 80–84 (2018).

Methods

Sample growth and characterizations. Single crystals of FeSn were grown using a chemical vapour transport technique with I_2 as a transport agent. Fe powder (Alfa Aesar, 99.998%) and Sn powder (Sigma Aldrich, 99.99%) were loaded in a quartz tube with ~3 mg cm^{-3} I_2. The evacuated quartz tube was put in a temperature gradient of from 520 °C (source) to 680 °C (sink) in a horizontal three-zone furnace. Thin plate-like, hexagonal single crystals were obtained, with a typical growth duration lasting from three weeks to one month. The phase of the grown crystals was confirmed with powder X-ray diffraction. Basic transport properties were measured with a standard five-probe configuration in a commercial cryostat.

Angle-resolved photoemission spectroscopy experiments. ARPES experiments were performed at two different synchrotron beamlines: the main data were acquired at Beamline 7 (MAESTRO) of the Advanced Light Source, and preliminary experiments were conducted at Beamline 21-ID-1 (ESM-ARPES) of the National Synchrotron Light Source II. The two ARPES endstations are respectively equipped with R4000 and DA30 hemispherical electron analysers (Scienta Omicron). FeSn samples were cleaved inside an ultrahigh vacuum chamber with a base pressure better than 4×10^{-11} torr. The ARPES data were acquired within 6 h after cleaving to minimize the effect of surface degradation. All datasets were collected at 20 K, except the one in Supplementary Fig. 5a, which was collected at 80 K. The lateral size of the beam was smaller than $20\times10\,\mu m^2$. Fermi surfaces and energy–momentum dispersions presented in Fig. 2, Supplementary Fig. 12 and Supplementary Fig. 14 were acquired with 92 eV and 140 eV photons, which maximize the visibility of Dirac bands. We mainly used LH polarized photons unless otherwise specified. The energy and momentum resolutions were better than 20 meV and 0.01 Å^{-1} respectively. Photon energy dependences in Supplementary Fig. 5 were scanned from 80 eV to 150 eV, which covers the complete Brillouin zone of FeSn in the k_z direction.

X-ray photoelectron spectroscopy. XPS experiments were conducted at Beamline 7 (MAESTRO) of the Advanced Light Source using an R4000 hemispherical electron analyser (Scienta Omicron). XPS spectra were measured on the same in situ cleaved samples on which the ARPES experiments were conducted. Before acquiring XPS spectra, we optimized beam position to a large single domain by monitoring the clarity of ARPES spectra. The XPS experimental geometry was such that the analyser was placed normal to the sample surface, while the beam came from 55° with respect to the sample normal. We acquired XPS spectra from seven different FeSn samples: four of them represent Sn termination, while the other three represent kagome termination (see Supplementary Fig. 2 for the full dataset). For comparison, we also acquired XPS spectra of Fe_3Sn_2 under the same conditions (see Supplementary Fig. 2 for detailed comparison).

Magneto-quantum oscillations. The magneto-quantum oscillation experiments were performed at the National High Magnetic Field Laboratory. Temperature and angular dependences of the oscillations were examined to reveal the effective mass and dimensionalities of the Fermi surfaces of interest.

The dHvA effects in the magnetic torque were measured using piezoresistive cantilevers (Seiko PRC-400 at the DC field facility and Seiko PRC-150 at the pulsed field facility) under ^{3}He or ^{4}He atmosphere. No signature of a magnetic phase transition was observed up to 65 T, and the transverse magnetization perpendicular to the applied field was estimated to be less than $0.0025\,\mu_B$ per Fe, implying a minimal change in the magnetic structure at high fields where oscillations were observed. We performed additional in-house torque measurements in a superconducting magnet using both capacitive (Cu:Be foil, 10–25 μm) and piezoresistive (SCL Sensortech PRSA-L300) cantilevers.

The SdH oscillations were observed in magnetoresistance on a thin piece of crystal (~6 μm thick) structured with focused ion beam, and the measurements were performed in DC fields up to 35 T with ^{3}He atmosphere. The focused ion beam fabrication was performed with a FEI Helios Nanolab 600 dual beam microscope with a Ga ion beam flux of 21 nA at a magnification of 350.

The oscillatory patterns of both dHvA and SdH oscillations were analysed with fast Fourier transform as a function of inverse fields. Each set of oscillatory amplitude was modulated by both the thermal and Dingle (residual impurity scattering) damping factors $R^i_T R^i_D$. Here i labels the i-th band, the thermal damping factor is given by $R^i_T = \frac{2\pi^2 k_B T m^*_i}{\hbar e B} \sinh^{-1}(\frac{2\pi^2 k_B T m^*_i}{\hbar e B})$ and the Dingle damping factor is given by $R^i_D = \exp[-\frac{2\pi^2 k_B T^i_D m^*_i}{\hbar e B}]$. The constants ħ and k_B are the reduced Planck constant and the Boltzmann constant, respectively. Fitting the temperature/field dependence of the oscillation (fast Fourier transform) amplitudes yields the effective mass m^* and Dingle temperature T_D. Here B is taken as the average field of the fast Fourier transform window from $B^{-1} = \frac{1}{2}(B^{-1}_{min} + B^{-1}_{max})$.

Bulk and surface electronic structure calculation from the first principles. DFT calculations were performed with the full-potential local-orbital (FPLO) code[41], version 18.00. The exchange and correlation energy was considered in the generalized gradient approximation using the parameterization of Perdew, Burke, and Ernzerhof (PBE-96)[42]. Self-consistent calculations were carried out using the four-component fully relativistic mode of FPLO. The following basis states were treated as valence states: Fe: 3*s*, 3*p*, 4*s*, 5*s*, 3*d*, 4*d* and 4*p*, and Sn: 4*s*, 4*p*, 4*d*, 5*s*, 6*s*, 5*d*, 5*p* and 6*p*. We used a linear tetrahedron method with 12×12×12 subdivisions in the full Brillouin zone for the bulk and 8×8×1 subdivisions for the slabs. The convergence level of the self-consistent spin density was better than 10^{-6} for the bulk and better than 10^{-4} for the slab calculations. We used the experimental structural data. Using the PYFPLO module of the FPLO package[41,43], we built a tight-binding Hamiltonian by projecting the Bloch states onto atomic-orbital-like Wannier functions associated with Fe 3*d* and 4*s* states, and Sn 5*s* and 5*p* states (Supplementary Fig. 15). We used this Hamiltonian to compute the Fermi surface, the dHvA spectrum and the k_z-integrated spectrum shown in Fig. 4. For the Wannier construction we used a mesh of 8×8×8 subdivisions in the full Brillouin zone.

To simulate the [001] surface state, slabs of various thickness, ranging from four atomic layers (one antiferromagnetic unit cell with two kagome layers and two Sn layers) to 16 atomic layers (four antiferromagnetic unit cells with eight kagome layers and eight Sn layers) were considered. In all cases, we fixed a vacuum of 1.7924 nm, which is four times the lattice parameter c, and kept the atomic distances and bond angles as in the bulk. The slabs were terminated with a kagome layer on one side and a Sn layer on the other side. Thus, they were stoichiometric and their electronic structure could be projected to either termination. We also have considered symmetric slabs (both sides terminated with either Sn or kagome layers) with nonstoichiometric compositions, which yield consistent results (see Supplementary Fig. 16).

We also performed total energy calculations to estimate the cleavage energy using a k mesh with 24×24×1 subdivisions. We found convergence of the cleavage energy with layer thickness for a slab with eight atomic layers. The calculated generalized gradient approximation cleavage energy amounted to 2.0 J m^{-2}, significantly larger than that of graphite (0.4 J m^{-2}) and smaller than that of the isotropic 3D metallic compound FeAl (6 J m^{-2}). We conclude that, from a chemical point of view, FeSn is not a 2D system but may be called an anisotropic 3D system. This conclusion is supported by similar band dispersions within the x–y plane (Γ-M-K-Γ) and perpendicular to that plane (Γ-A, L-M, K-H) as shown in Supplementary Fig. 10.

Data availability

The data that support the plots within this paper and other findings of this study are available from the corresponding author upon reasonable request.

Code availability

The codes used for the DFT and tight-binding calculations in this study are available from the corresponding authors upon reasonable request.

References

41. Koepernik, K. & Eschrig, H. Full-potential nonorthogonal local-orbital minimum-basis band-structure scheme. *Phys. Rev. B* **59**, 1743–1757 (1999).
42. Perdew, J. P., Burke, K. & Ernzerhof, M. Generalized gradient approximation made simple. *Phys. Rev. Lett.* **77**, 3865–3868 (1996).
43. Koepernik, K. FPLO (IFW Dresden, 2018).

Acknowledgements

We are grateful to C. Felser, S. Borisenko, M. Knupfer, K. Koepernik, L. Levitov and A. Fahimniya for fruitful discussions. M.P.G., J.-S.Y., J.I.F., S.F., M.R. and J.v.d.B. thank U. Nitzsche for technical assistance in maintaining computing resources at IFW Dresden. R.C. acknowledges support from the Alfred P. Sloan Foundation. This research was funded, in part, by the Gordon and Betty Moore Foundation EPiQS Initiative, Grant no. GBMF3848 to J.G.C. and ARO Grant no. W911NF-16-1-0034. M.K., L.Y., S.F., E.K. and M.P.G. acknowledge support by the STC Center for Integrated Quantum Materials, NSF grant number DMR-1231319. M.K. acknowledges support from the Samsung Scholarship from the Samsung Foundation of Culture. L.Y. acknowledges support from the Tsinghua Ed fucation Foundation. The computations in this paper were run on the ITF/IFW computer clusters (Dresden, Germany) and Odyssey cluster supported by the FAS Division of Science, Research Computing Group at Harvard University. M.R and J.v.d.B. acknowledge support from the German Research Foundation (DFG) via SFB 1143, project A5. M.P.G. thanks the Alexander von Humboldt Foundation for financial support through the Georg Forster Research Fellowship Program, Germany. J.-S.Y. and J.I.F. thank the IFW excellence programme. This research used the resources of the Advanced Light Source, a US Department of Energy (DOE) Office of Science User Facility under contract no. DE-AC02-05CH11231. A portion of this work was performed at the National High Magnetic Field Laboratory, which is supported by the National Science Foundation Cooperative Agreement no. DMR-1644779, the State of Florida and the DOE. Pulsed magnetic field measurements were supported by the DOE BES 'Science at 100 T' grant. Operation of the ESM beamline at the National Synchrotron Light Source is supported by DOE Office of Science User Facility Program operated for the DOE Office of Science by Brookhaven National Laboratory under Contract no. DE-AC02-98CH10886. D.C.B. acknowledges use of the Center for Nanoscale Systems, a member of the National Nanotechnology Coordinated Infrastructure Network, which is supported by the National Science Foundation under NSF award no. 1541959. J.v.d.B. was supported by the DFG through the Wurzburg-Dresden Cluster of Excellence on Complexity and Topology in Quantum Matter - ct.qmat (EXC 2147, project ID 39085490).

Author contributions

M.K. performed the ARPES experiment and analysed the resulting data while A.L., C.J., A.B., E.R., K.K. and E.V. assisted. L.Y. synthesized and characterized the single crystals and performed the quantum oscillation experiments while M.K.C., R.D.M. and D.G. assisted. M.P.G. and S.F. performed the theoretical calculations while J.-S.Y., J.I.F. J.v.d.V., M.R. and E.K. assisted. M.H. and M.K. conducted the AFM measurements. D.C.B. performed the electron microscopy study. All authors contributed to writing the manuscript. J.G.C. and R.C. supervised the project.

Competing interests

The authors declare no competing interests.

Additional information

Supplementary information is available for this paper at https://doi.org/10.1038/s41563-019-0531-0.

Correspondence and requests for materials should be addressed to J.G.C. or R.C.

Reprints and permissions information is available at www.nature.com/reprints.